Neutron Scattering from Quantum Materials with the Spallation Neutron Source

By Jonathan Gaudet and Bruce D. Gaulin

Spallation neutron sources, based on accelerators rather than nuclear reactors, were proposed in the 1960s and then developed in the 1970s. Canadians were at the vanguard of such sources when the Intense Neutron Generator was proposed for Chalk River; unfortunately, it was never funded. Both the Intense Pulsed Neutron Source at Argonne National Laboratory, and the ISIS Pulsed Neutron Source at the Rutherford Appleton Laboratory in the UK ran successful user programs based on spallation neutron sources as early as the 1980s. However, the Spallation Neutron Source (SNS) at Oak Ridge National Laboratory in the USA, which has operated now for just over 10 years, has ushered in a very large expansion in our capabilities to carry out forefront neutron scattering experiments on a wide variety of materials using such a source.

Most of these new measurements are performed using the time-of-flight of the neutron. The neutron is a massive particle (in contrast to photons) so one can measure the energy of a neutron by measuring its speed. New "chopper" inelastic spectrometers are designed to do exactly this, and they are designed to do so while being very efficient with the scattered neutrons. They aim to measure neutrons scattered into a large fraction of 4π steradians of scattered solid angle, and with time, and hence energy, so as to ultimately determine the scattering function, $S(\mathbf{Q},\hbar\omega)$, as comprehensively as possible. $S(\mathbf{Q},\hbar\omega)$ is directly related to the scattered neutron intensity and informs on the correlations between magnetic moments in solids in both space (through $\mathbf{Q}$) and time (through $\hbar\omega$). $\mathbf{Q}$ is the momentum or wavevector transfer of the scattering event, while an amount of energy $\hbar\omega$ is simultaneously transferred from the incident neutron to the sample or vice-versa. A schematic diagram of a chopper inelastic spectrometer is shown in Fig. 1.

Summary

Modern neutron time-of-flight spectroscopy allows a full understanding of complex condensed matter systems. Here, we present several examples related to superconductivity and quantum magnetism.

These advances in neutron instrumentation are almost certain to continue unabated, and even accelerate, as the international community has been very busy building up related neutron capabilities at JPARC in Japan, at the Chinese Spallation Neutron Source (which just turned on) and at the European Spallation Source (scheduled for completion in the early 2020s). Taken together, these international user facilities represent a reinvestment in neutron scattering infrastructure of ~$9B. With new experimental capabilities come new possibilities, and indeed neutron scattering studies are possible today, that would have been unimaginable 10 years ago. The new capabilities can be used in a variety of ways. For example, we can measure weaker signals, smaller crystals, or employ more extreme sample environments, and we can do all of this while obtaining a comprehensive dynamic structure function $S(\mathbf{Q},\hbar\omega)$, even with polarization analysis in favourable conditions.

Several of these issues come to bear in the study of new quantum materials. Quantum materials are often new magnets and superconductors, and sometimes both, where the fundamental degree of freedom in the material is inherently quantum mechanical in nature. The magnetic moments in the new magnetic materials can exhibit strong quantum fluctuations when the quantum numbers describing the moments are small, such as $S = 1/2$. This arises, for example, from the magnetism associated with a single unpaired electron in the d-shell of Cu^{2+}, as occurs in the cuprate-based high Tc superconductors. However it can also arise due to the effects of crystalline electric fields in f-electron rare earth magnets, such as the pyrochlore magnets $Er_2Ti_2O_7$ and $Yb_2Ti_2O_7$. Measurements on both of these types of systems will be described below. What makes such measurements difficult, is that the low quantum numbers tend to produce small magnetic moments in solids, and hence weak signals, as the magnetic neutron scattering cross section goes like the μ^2. To make matters worse, new quantum materials, like almost all new materials, tend to be initially produced as small single crystals. Finally, at least in the case of the high Tc cuprates, the energy scale for the magnetism is very large, and hence the inelastic scattering, which the chopper spectrometers are designed to measure, tends to be distributed over a large dynamic range in energy. Nonetheless, new neutron sources and instrumentation leave us much

Jonathan Gaudet <gaudej@mcmaster.ca>

and

Bruce D. Gaulin, <gaulin@mcmaster.ca>,

Department of Physics and Astronomy, Brockhouse Institute for Materials Research McMaster University, Hamilton, ON L8S 4M1

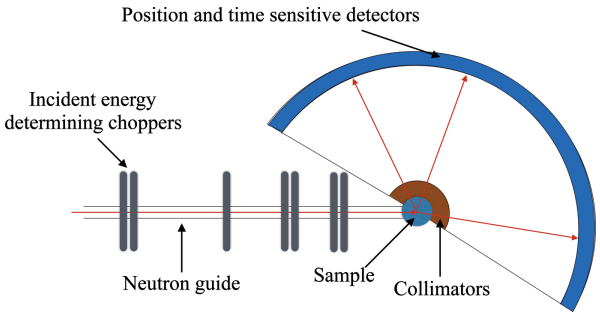

Fig. 1 A schematic diagram of a modern neutron time-of-flight chopper spectrometer is shown. A train of monochromatic neutron pulses is selected by a series of phased choppers, and this incident beam is delivered to the sample. The scattered neutrons are collected as a function of time-of-arrival and position on the detectors banks, allowing the measurement of the dynamic structure function $S(\mathbf{Q}, \hbar\omega)$. The array of position and time sensitive detectors is two dimensional (coming out of the page) so as to provide coverage over as much of 4π steradians in solid angle as possible.

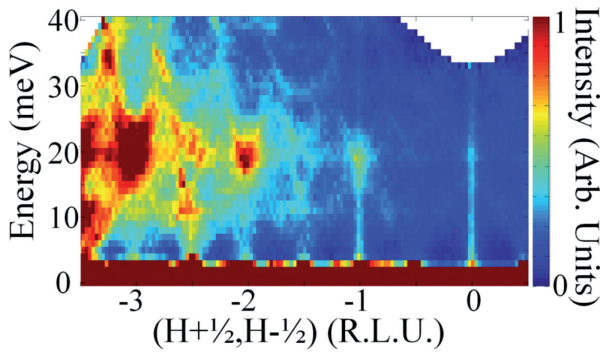

Fig. 2 Inelastic neutron scattering spectra from $La_{(2-x)}Ba_{(x)}CuO_4$ with $x = 0.035$ obtained with the ARCS time-of-flight spectrometer and a neutron incident energy of 60 meV is shown for a temperature of 5 K. Spin wave excitations are most visible at low **Q** and can be seen centered around (1/2 −1/2) and (−1/2 −3/2). Phonon excitations are most visible at high momentum transfer **Q**. Hybridized spin-phonon excitations occur at the crossing of the spin wave excitations and optic phonon excitations, centered around 20 meV.

better "armed" to address these technical challenges, and indeed great progress in the study of new quantum materials with neutrons is being made.

In what follows, we discuss three such recent examples of neutron scattering studies from quantum materials carried out under the auspices of "Canadian Participation at the Spallation Neutron Source". These examples are three of many Canadian experiments carried out at SNS; they are chosen from our own portfolio of results for convenience only. This $15M CFI International Access Fund project was awarded to McMaster University in 2003, and it gave Canadian scientists involvement in the design of two SNS instruments (SEQUOIA and VULCAN), and provided Canadian neutron scatterers enhanced access to these cutting edge capabilities for 10 years. This agreement with SNS concluded at the beginning of 2018. Nonetheless it has been a great success in maintaining Canada at the forefront of neutron expertise, and has had a disproportionate impact on the study of new quantum and frustrated magnets, and these are the subjects of the studies described below.

SPIN AND PHONON EXCITATIONS IN A PROTOTYPICAL HIGH-T_C SUPERCONDUCTOR PARENT COMPOUND

Hole-doped, cuprate-based high temperature superconductors can be thought of as quasi-two-dimensional quantum magnets, based on magnetic moments derived from a single d-level electron in Cu^{2+}, with mobile-hole impurities [1]. In their pristine form, without impurities, materials like $La_{(2-x)}Ba_{(x)}CuO_4$ with $x = 0$, are very strong antiferromagnets with ordered states forming near $T_N \sim 300$ K. However, the mobile impurities break down the commensurate, quasi-two-dimensional antiferromagnetic ordered state very quickly, by $x \sim 0.02$. At the impurity concentrations for which superconductivity is established, $x > 0.05$, the magnetism is incommensurate, consistent with the "stripe" picture of high temperature superconductivity, and it is also highly dispersive, meaning that the spin excitation spectrum is centred on wave vectors such as (1/2,1/2,L), and disperses to high energies, ~200 meV.

As new time-of-flight neutron instrumentation employs large arrays of position sensitive detectors, neutron scattering processes are detected across a large range of three-dimensional momentum space, **Q,** and such measurements give large coverage in reciprocal space. The neutrons' time-of-arrivals at the detectors are also recorded, and this provides the energy transfer of the scattering events, $\hbar\omega$. The data set in Fig. 2, which shows the neutron inelastic spectra of $La_{(2-x)}Ba_{(x)}CuO_4$ with $x = 0.035$, was obtained with the time-of-flight chopper spectrometer ARCS at the SNS using an incident neutrons energy of 60 meV [2]. The total scattering spectra obtained from ARCS gives a 4-dimensional (3 **Q** dimensions and 1 energy dimension) data set. However, it is difficult to analyze or even look at 4-dimensional data sets, and hence the resulting neutron scattering spectra shown in Fig. 2 is the result of two different integrations within reciprocal space of this 4 dimensional data set. For this particular example, integrations along the [H,−H,0] and the [0,0,L] directions in reciprocal space have been performed, revealing inelastic scattering as a function of energy, plotted along the [−H,−H,−4 < L < 4] direction in reciprocal space.

Figure 2 illustrates the approximate separation of the inelastic signal, with spin excitations at relatively low **Q**, and phonon or lattice vibration scattering at relatively large **Q**. The spin excitations are identified as the very dispersive, almost vertical rods of inelastic scattering, emanating out of the (1/2, −1/2, −4 < *L* < 4) and (−1/2,−3/2,−4 < *L* < 4) positions in reciprocal space. In contrast the phonons give much stronger intensity at larger **Q**, and their dispersion is more complex. This approximate separation of spin and phonon scattering, according to low and high **Q**, is due to the fact that neutron scattering from phonons goes like $\mathbf{Q}^2$, while the magnetic neutron scattering cross section goes like the square of the magnetic form factor, which falls off at high **Q**. For this reason, the phonons can be inferred from Fig. 2 and correspond to features whose intensity grows as a function of **Q**, such as the acoustic phonons centred at (−1,−2, −4 < *L* < 4). Multiple optic phonon branches are also observed and correspond, for example, to the non-dispersive excitations centred around 20 and 30 meV.

Since both phonon and spin-wave excitations can be simultaneously measured and analyzed from scattering spectra such as the one shown in Fig. 2, one can also infer the existence of more exotic excitations. For $La_{(2-x)}Ba_{(x)}CuO_4$, an intriguing feature in these experiments is the very large enhancement of scattered intensity (or resonance-like scattering) observed at the crossing of the highly dispersive or "vertical" spin wave dispersions originating from wave vectors such as (1/2, −1/2, −4 < *L* < 4) and (−1/2, −3/2, −4 < *L* < 4), and the ~ "horizontal" optic phonons centred at 20 meV. Such an enhancement is attributed to a hybridized spin-phonon excitation as it occurs at their crossing in **Q** and $\hbar\omega$ space. Density functional theory for the phonons in $La_{(2-x)}Ba_{(x)}CuO_4$ reveals that the particular optic phonon involved in this process, near 20 meV, corresponds to vibrations of the oxygen ions localized between the Cu^{2+} ions. The magnetic exchange interaction strength in $La_{(2-x)}Ba_{(x)}CuO_4$ comes from strong super-exchange between neighbouring Cu^{2+} ions, mediated by the O^{2-} ions. Flexing this Cu^{2+}- O^{2-}-Cu^{2+} bond, through this optic phonon, is expected to couple directly to the magnetism in this system. Thus a strong magneto-elastic coupling is perhaps not unexpected. Nonetheless, observing such a subtle effect requires rather comprehensive $S(\mathbf{Q},\hbar\omega)$ information and new time-of-flight chopper spectrometers are very well suited to providing such data on systems of interest. Our measurements have shown that such coupling between the spin excitation spectrum and the phonons in $La_{(2-x)}Ba_{(x)}CuO_4$ extends across x to at least $x = 0.11$, and it is therefore a general physical characteristic of this important family of quantum materials [3].

THE SPIN GLASS GROUND STATE IN THE RANDOM BILAYER QUANTUM ANTIFERROMAGNET $LuCoGaO_4$

The comprehensive nature for which $S(\mathbf{Q}, \hbar\omega)$ can be measured using chopper spectrometers and a spallation source really comes into its own for the study of disordered materials. In the case of magnets with disordered ground states, such as spin glass states, comprehensive coverage of $S(\mathbf{Q}, \hbar\omega)$ is very important as the magnetic scattering is itself distributed in **Q** and $\hbar\omega$, rather than organized into sharp, three dimensional Bragg peaks, and spin excitations with well-defined energies and momenta, as occurs in ordered magnets. A spin glass ground state is typically stabilized by the combination of structural disorder and competing interactions, such that a frozen, disordered magnetic state results at low temperatures. This is illustrated below for the random-bilayer spin-glass $LuCoGaO_4$, using the SEQUOIA chopper spectrometer at the SNS [4].

$LuCoGaO_4$ possesses a hexagonal crystal structure with magnetic Co^{2+} ions and nonmagnetic Ga^{3+} ions randomly occupying triangular bilayers in a 1:1 ratio. The single ion ground state of the Co^{2+} ions gives rise to an effective quantum spin-1/2 moment that interacts antiferromagnetically with its random two-dimensional network of neighbouring Co^{2+} ions. This material therefore has the key ingredients necessary to stabilize a spin glass ground state − frustrated antiferromagnetic interactions on triangular lattices and structural randomness.

While the spin glass ground state lacks long range order, it does possess frozen, short range order at low temperatures. The elastic magnetic neutron scattering shown in Fig. 3 illustrates how this appears in such a spin glass state. In both Fig. 3(a) and (b), $S(\mathbf{Q}, \hbar\omega)$, integrated in energy from −1 to 1 meV in order to isolate the elastic scattering, is shown. In (a), an additional integration have been performed along the [0,0,*L*] direction (from −2.75 to 2.75 in reciprocal lattice units) so as to reveal the static spin correlations occurring within the triangular bilayers occupied by the Co^{2+} and Ga^{3+} ions. Examination of these data sets for $LuCoGaO_4$ obtained at different temperatures reveals that the static spin correlations build up near **Q** = (1/3,1/3,0) and equivalent wave vectors, starting at temperatures as high as $T \sim 120$K, which corresponds to the Curie-Weiss temperature of this system. The **Q** = (1/3,1/3,0) wave vector indicates a local magnetic structure. A long range ordered version of this magnetic structure is known to exist, for example, in $YbFe_2O_4$ in the absence of structural disorder. The width of these "quasi-Bragg peaks" are indicative of the short range order of the $LuCoGaO_4$ ground state. The correlation length within the **a-b** plane (the plane of the bilayers) is related to the inverse of the width of these quasi-Bragg peaks. Analysis reveals that the correlation length, ξ, increases from about 2-3 Å at 120K to 6.5-7.5 Å by ~19K, which corresponds to the spin-glass transition in $LuCoGaO_4$. On further lowering the temperature from 19K to 1.8K, the correlation length saturates at this small value, consistent with the spin freezing of this system. Finally, Fig. 3(a)) shows that the width of each quasi-Bragg peak is independent of the direction of **Q** within the [*H*,*H*,0]/[*H*,*H*,0] plane, and therefore ξ is isotropic within the triangular bilayers of $LuCoGaO_4$.

In Fig. 3(b), $S(\mathbf{Q},\hbar\omega)$ for $LuCoGaO_4$ is once again shown with an integration in energy from −1 meV to 1 meV, hence picking

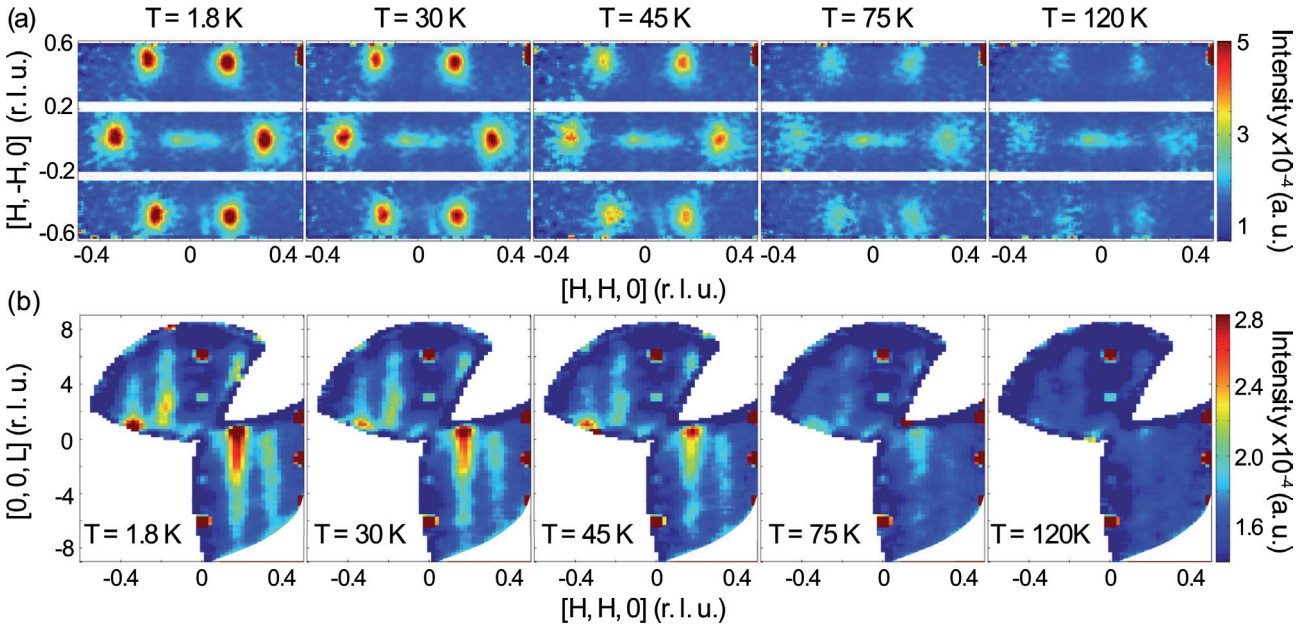

Fig. 3 (a) shows the elastic neutron scattering spectra from LuCoGaO4 within the $[H,-H,0]$-$[H,H,0]$ plane. (b) reveals the scattering spectra within the $[H,H,0]$-$[0,0,L]$ plane. The appearance of "rods" of scattering along $[0,0,L]$ are indicative of two dimensional correlations. Both data sets are presented for temperatures ranging from 1.8K to 120K, both above and below the spin freezing temperature of LuCoGaO4 (~19K), and up to the ~Curie-Weiss temperature of this system (~100K).

up elastic scattering only, but now with a **Q** integration along the $[H,-H,0]$ direction. This particular plane of the four-dimensional $S(\mathbf{Q},\hbar\omega)$ shows elastic scattering within the $[H,H,0]/[0,0,L]$ plane of reciprocal space, and therefore informs on static spin correlations arising between the bilayers. The scattering spectra shown in Fig. 3(b) for $LuCoGaO_4$ at 1.8K reveals rods of scattering along $(0,0,L)$ that are centered at $\mathbf{Q} = (1/3,1/3,L)$. The rod-like shape of these features is typical of the two-dimensional nature of the spin correlations, indicating that little or no correlations exist between the different Co/Ga bilayers, even at the lowest temperatures measured. We thus conclude that the spin glass state in $LuCoGaO_4$ is intrinsically two dimensional in nature.

SPIN ANISOTROPY AND S_{EFF} = 1/2 QUANTUM MOMENTS IN RARE EARTH PYROCHLORE MAGNETS

While triple-axis spectroscopy is still widely used to study excitations in solids, inelastic neutron scattering with triple axis instruments at high energy transfers, say above 30 meV, is relatively challenging. However, such measurements are routinely performed using time-of-flight techniques and instrumentation, such as the SEQUOIA chopper spectrometer at the SNS. The combination of a forefront spallation neutron source and a forefront chopper spectrometer such as SEQUOIA allows routine neutron spectroscopic measurements with energy transfers in the 100s of meV regime, and up to the 2-3 eV regime if required. This "high energy physics" is vital in condensed matter physics as it informs on the single-ion properties of the atoms and ions that constitute a specific material. For example, it is known that the single-ion properties of the magnetic ions in the frustrated rare-earth (RE) pyrochlore magnets $RE_2M_2O_7$ strongly influence the magnetic ground states of these systems, as these properties determine both the spin anisotropy and the moment at the magnetic RE site.

Within the cubic pyrochlore structure, both the RE and M sublattices correspond to a network of corner-sharing tetrahedra. Due to the triangular motif that forms each tetrahedron, the pyrochlore lattice is the archetype example of geometrical frustration in three dimensions. This geometrical frustration makes pyrochlore magnets amenable for the realization of new exotic magnetic ground states [5]. For this reason, they have attracted intense and sustained interest in the condensed matter community. A key ingredient for the stabilization of the different observed magnetic states is the local spin anisotropy of the rare-earth moments that results from their single-ion physics. In pyrochlore magnets, as shown in Fig. 4a, the rare-earth moments sit at the centre of a distorted cube of O^{2-} ions and the spin anisotropy is defined locally using the axis that connects the centres of two adjacent tetrahedra. Ising or unidirectional anisotropy is stabilized if the spins can only point into or out of the centre of the tetrahedra on which a spin resides (e.g., the red spin in Fig. 4(a)). XY or planar anisotropy results from spins constrained to lie within a plane perpendicular to the Ising axis

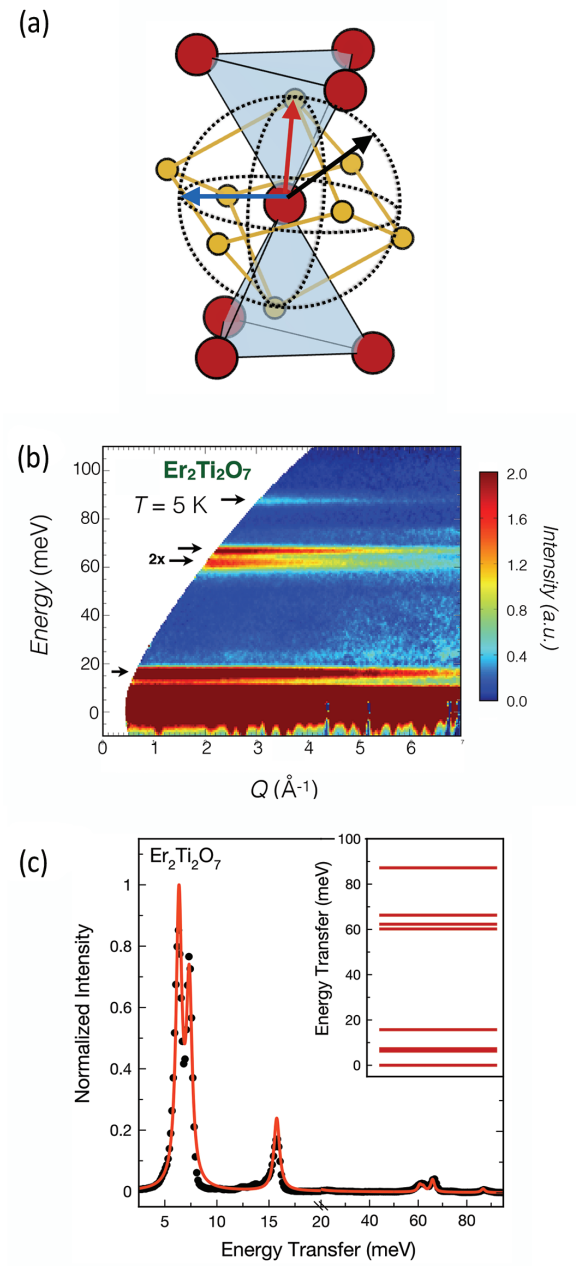

Fig. 4 (a) The local environment of the rare-earth ions within the pyrochlore magnet. The yellows dots correspond to the oxygen ions arranged on a distorted cube and the red dots correspond to the rare-earth ions. The red spin displays typical Ising anisotropy, while the blue spin is indicative of XY anisotropy and the black spin is typical of a Heisenberg system. (b) shows the neutron inelastic spectra of $Er_2Ti_2O_7$ obtained using the SEQUOIA time-of-flight spectrometer with incident neutrons of energy 150 meV. (c) shows the resulting CEF fit to the inelastic scattering from $Er_2Ti_2O_7$ and the excellent agreement between the calculation (red line) and the experimental data (black dots). The inset to (c) shows the CEF energy scheme for Er^{3+} in $Er_2Ti_2O_7$.

(e.g., the blue spin in Fig. 4(a)). If the spins are isotropic, that is if they lack anisotropy, such a system is referred to as Heisenberg in nature and its spins are free to point anywhere in three dimensional space (e.g., the black spin in Fig. 4(a)). Which spin anisotropy a given rare earth pyrochlore magnet displays depends on the exact details of the degeneracy breaking of the (2J+1) manifold of its spin-orbit ground state. The lifting of this degeneracy occurs due to interaction between the magnetic ion and the crystalline electric field originating from its local environment of neighbouring ions. A determination of the exact crystal electric field (CEF) Hamiltonian is possible using inelastic neutron scattering via a detailed analysis of the transition energies between different CEF levels, as well as their respective scattered intensities. As the strength of the CEFs in the rare earth pyrochlores is on the order of 50-100 meV, the determination of the spin anisotropy through the detailed characterization of the CEF Hamiltonian of rare earth pyrochlore magnets is perfectly suited for the time-of-flight SEQUOIA spectrometer at SNS.

To illustrate the analysis of neutron spectroscopy that leads to the determination of the local spin anisotropy, and the size of the magnetic moment within the CEF ground state, we focus on the particular case of $Er_2Ti_2O_7$ [6]. In this material, the magnetic erbium ions have a 3^+ oxidation state with an electronic configuration corresponding to $[Xe]4f^{11}$. Following Hund's rules, the spin-orbit ground state then has total angular momentum J = 15/2 with $L = 3$ and $S = 2$ and is $(2J+1) = 16$ fold degenerate. Kramer's theorem stipulates that each CEF level should be at least doubly degenerate, which implies that a maximum of 8 different CEF states can be obtained. The exact symmetry of the CEF Hamiltonian appropriate for this Er^{3+} site predicts that the complete degeneracy of the 8 CEF states should be lifted. Thus, at a temperature that is sufficiently low to only thermally populate the CEF ground state, 7 inelastic transitions from the CEF ground state to CEF excited states should be observed, and these will fully determine the entire CEF manifold.

The inelastic spectra of $Er_2Ti_2O_7$ is shown in Fig. 4(b) for a neutron incident energy of 150 meV and a temperature of 5K. The first excited CEF doublet of $Er_2Ti_2O_7$ is located at around 6 meV (~70K) which implies that the inelastic spectra shown in Fig. 4(b) should only involve CEF transitions originating from the CEF ground state. The magnetic CEF excitations can be identified by analyzing the **Q** dependence of the inelastic features appearing in Fig. 4(b). Indeed, the intensity of a magnetic excitation, as compared to phonons, should decrease in intensity as a function of the momentum transfer **Q**. From Fig. 4(b), it is clear that the features around 15, 65, 70 and 90 meV correspond to CEF excitations. For this specific analysis, inelastic spectra using 25 meV and 90 meV incident neutron energy have also been collected and revealed that the feature around 15 meV in Fig. 4(b) corresponds to three different CEF levels. Furthermore, the feature around 60 meV in Fig. 4(b) is in fact, two closely space CEF excitations. These five CEF excitations, along with the CEF excitations observed in Fig. 4(b) around 70 meV and 90 meV reveal the energies of all of the excited

CEF levels, and a robust CEF Hamiltonian can be determined for $Er_2Ti_2O_7$.

The CEF Hamiltonian (H_{cef}) for $Er_2Ti_2O_7$ can be derived using the Stevens formalism [7]. This formalism consists of writing the Coulomb potential of the CEF in terms of Stevens operators (O_{nm}) made up from J_z, J_+ and J_- operators. For the pyrochlore structure, the point-group symmetry of the Er^{3+} site is D_{3d}, and the CEF Hamiltonian consists of six Stevens operators: O_{20}, O_{40}, O_{43}, O_{60}, O_{63} and O_{66} (e.g., $O_{20} = 3J_z^2 - J(J+1)$). Each Stevens operator is unit-less, but is multiplied by a CEF parameter B_{nm} ($H_{cef} = \sum B_{nm} O_{nm}$). The energy distribution of the CEF levels, as well as the composition of each CEF eigenvector, depends on the B_{nm} parameters. Fitting of the CEF parameters B_{nm} can be performed using the energies of the CEF transitions observed via neutron spectroscopy as shown in Fig. 4(b). Further constraints are provided by the relative intensity of each of the CEF transitions. The result of the fitting procedure is shown in Fig. 4(c) where this CEF calculation is reproduced along with the experimentally-derived inelastic neutron scattering spectra for $Er_2Ti_2O_7$ at low temperature. Excellent agreement between the calculation and the neutron scattering experiment is obtained, validating the determination of the CEF Hamiltonian for $Er_2Ti_2O_7$.

With the CEF Hamiltonian for $Er_2Ti_2O_7$ in hand, it is possible to calculate the strength of the local g-tensor, parallel ($g_{\|}$) and perpendicular (g) to the Ising axis, and this will determine the local anisotropy of the Er^{3+} moment. As we are interested in the ground state properties of this material, the g-tensor anisotropy can be computed solely using the composition of the CEF ground state doublet. This procedure leads to $g_{\|} = 3.9$ and $g = 6.3$, implying that the CEF ground state doublet of $Er_2Ti_2O_7$ has XY anisotropy, and its spins have a preference to lie within a plane perpendicular to the local Ising axis. It also allows us to conclude that the eigenfunction making up the CEF ground state doublet is mostly made up of $m_J = 1/2$, and hence the moments in $Er_2Ti_2O_7$ correspond to quantum degrees of freedom. This XY or planar anisotropy helps stabilize antiferromagnetic long-range magnetic order in $Er_2Ti_2O_7$ with the Er^{3+} spins pointing within the XY local plane. The ground state selection of this particular XY spin structure is proposed to originate from a novel order-by-disorder mechanism [8], which selects a particular ordered magnetic structure due to it's propensity to fluctuate, as opposed to the usual propensity to lower its energy. This entropic selection is rare in nature, but is possible in $Er_2Ti_2O_7$ due to a well isolated CEF ground state doublet with an effective spin 1/2, XY anisotropy and the high symmetry of the pyrochlore structure.

CONCLUSION

Neutron scattering techniques are of fundamental importance to the study of condensed matter physics, as they measure $S(\mathbf{Q},\hbar\omega)$ across entire Brillouin zones and over energies of relevance to elementary excitations in solids. New quantum materials present challenges for neutron scattering, as their quantum degrees of freedom often correspond to small magnetic moments originating from low quantum numbers. New spallation neutron sources and new instrumentation based on the time-of-flight of the neutron have vastly expanded our capabilities to perform meaningful neutron experiments on such systems. We illustrated this with three recent examples taken from Canadian work at the Spallation Neutron Source at Oak Ridge National Laboratory. These examples focused on quantum magnetism and its interactions with phonons in a prototypical high temperature superconducting parent material; on a disordered quasi-two dimensional spin glass; and on the use of high energy neutron spectroscopy to determine the local spin anisotropy and moment size in a rare earth-based pyrochlore magnet.

REFERENCES

1. M. Fujita, H. Hiraka, M. Matsuda, M. Matsuura, J.M. Tranquada, S. Wakimoto, G. Xu, and K. Yamada, "Progress in Neutron Scattering Studies of Spin Excitations in High-Tc Cuprates", *Journal of the Physical Society of Japan*, **81**, 011007 (2012).
2. J.J. Wagman, D. Parshall, M.B. Stone, A.T. Savici, Y. Zhao, H.A. Dabkowska, and B.D. Gaulin, "Quasi-two-dimensional spin and phonon excitations in $La_{1.965}Ba_{0.035}CuO_4$", *Phys. Rev. B,* **91**, 224404 (2015).
3. J.J. Wagman, J.P. Carlo, J. Gaudet, G. Van Gastel, D.L. Abernathy, M.B. Stone, G.E. Granroth, A.I. Kolesnikov, A.T. Savici, Y.J. Kim, H. Zhang, D. Ellis, Y. Zhao, L. Clark, A.B. Kallin, E. Mazurek, H.A. Dabkowska, and B.D. Gaulin, "Neutron scattering studies of spin-phonon hybridization and superconducting spin gaps in the high-temperature superconductor", *Phys. Rev. B*, **93**, 094416 (2016).
4. K. Fritsch, K.A. Ross, G.E. Granroth, G. Ehlers, H.M.L. Noad, H.A. Dabkowska, and B.D. Gaulin, "Quasi-two-dimensional spin correlations in the triangular lattice bilayer spin glass $LuCoGaO_4$", *Phys. Rev. B*, **96**, 094414 (2017).
5. J.S. Gardner, M.J.P. Gingras, and J.E. Greedan, "Magnetic pyrochlore oxides", *Rev. Mod. Phys*. **82**, 53 (2010).
6. J. Gaudet, A.M. Hallas, A.I. Kolesnikov, and B.D. Gaulin, *Effect of Chemical Pressure on the Crystal Electric Field States of Erbium Pyrochlore Magnets*, *Phys. Rev. B*, **97**(2), 024415 (2018).
7. M. Hutchings, in Solid State Physics, Vol. 16, edited by F. Seitz and D. Turnbull, Academic Press, pp. 227-273 (1964).
8. L. Savary, K.A. Ross, B.D. Gaulin, J.P.C. Ruff, and L. Balents, "Order by quantum disorder in $Er_2Ti_2O_7$", *Phys. Rev. Lett.* **109**, 167201 (2012).